https://doi.org/10.1016/j.ensm.2020.06.015

Rich atomic interfaces between sub-1 nm RuO_x clusters and porous Co_3O_4 nanosheets boost oxygen electrolysis bifunctionality for advanced Zn-air batteries

Qian Lu [a], Yanan Guo [a], Peng Mao [b], Kaiming Liao [a, *], Xiaohong Zou [a], Jie Dai [a], Peng Tan [c, d], Ran Ran [a], Wei Zhou [a], Meng Ni [c], Zongping Shao [a, e, *]

[a] State Key Laboratory of Materials-Oriented Chemical Engineering,
College of Chemical Engineering, Nanjing Tech University, Nanjing 210009, China

[b] School of Physics and Astronomy, University of Birmingham,
Birmingham B15 2TT, United Kingdom.

[c] Department of Building and Real Estate, The Hong Kong Polytechnic University, Hung Hom, Kowloon, Hong Kong 999077, China

[d] Department of Thermal Science and Energy Engineering,
University of Science and Technology of China, Hefei 230026, Anhui, China

[e] Department of Chemical Engineering, Curtin University, Perth, WA 6845, Australia

* Corresponding Author,
E-mail addresses: kaimingliao@njtech.edu.cn; shaozp@njtech.edu.cn

Abstract: The practical use of Zn-air batteries (ZABs) is strongly dependent on the availability of bifunctional oxygen electrocatalysts that should have high activity and durability for both oxygen evolution/reduction reactions (OER/ORR) in alkaline solution. Herein, we report the design of a new Ru-based bifunctional catalyst characterized with rich atomic interfaces through the in-situ growth of sub-1nm RuO_x clusters on the surface of porous Co_3O_4 nanosheets with 4.1 *wt*% Ru loaded. Such unique architecture ensures the creation of high-energy interfacial Ru-O-Co bond that allows fine tuning of the electronic structure of both Ru and Co.

The as-prepared catalyst exhibits superior oxygen electrolysis bifunctionality, indicated by an ultralow potential gap of 0.71 V between the potential of OER at 10 mA cm^{-2} (1.51 V) and the half-wave potential for ORR (0.80 V). Remarkably, rechargeable ZAB with such electrocatalyst demonstrates not only high rate performance (50 mA cm^{-2}) and power density (150 mW cm^{-2}), but also superior round-trip efficiency (68.4%, after 250 h). X-ray photoelectron and Raman spectroscopy reveal that the active sites for ORR/OER are mainly the unsaturated trivalence Ru in RuO_x clusters, and the formed interfacial Ru-O-Co bond can avoid the dissolution of RuO_x in alkaline electrolyte, holding great potential in implementation of long-life rechargeable ZABs.

Keywords: Zn-air battery; bifunctional electrocatalyst; RuO_x cluster; Ru-O-Co bond; atomic interface.

1. Introduction

The quickly expanded demand of sustainable clean energy has triggered the rapid development of electrochemical energy storage and conversion technologies with high energy density and improved safety.[1-4] Compared to Li-ion batteries, rechargeable Zn–air batteries (ZABs) with high theoretical energy density of 1086 Wh kg^{-1}, low price of zinc anode, and high safety of aqueous electrolyte, are highly promising for large-scale energy storage if the durability and round-trip efficiency can be greatly improved.[5-8] Currently, unsatisfactory cycling stability, poor rating performance and low round-trip efficiency of the cell, which is mainly attributed to the insufficient air electrode performance, such as sluggish ORR and/or OER kinetics and poor durability, significantly hampers the practical use of ZABs.[9] For OER in alkaline solution, RuO_2 has been regarded as the benchmark electrocatalyst, and the price of Ru is also economically advantageous compared to Pt (only about 4%).[10, 11] However, RuO_2 suffers slow dissolution in alkaline solution, resulting in unsatisfactory durability.[12-14] In addition, the ORR activity of Ru-based catalysts is usually very poor. Therefore, cost-competitive Ru-based compounds, by themselves, have been seldomly applied as bifunctional catalysts in rechargeable ZABs.

The formation of composite from heteroatom-doped carbon and transition metal compound is extensively applied strategy to construct bifunctional oxygen electrocatalysts. Recently, many transition metal compound/heteroatom-doped carbon composites have been developed as alternative bifunctional oxygen electrocatalysts, in which the heteroatom-doped carbon usually serve as ORR electrocatalyst and the transition metal compound provides active sites for OER process.[15-19] For example, our group reported a bifunctional oxygen catalyst with CoS_x particle embedded in nitrogen-doped carbon, in which the CoS_x served as OER active sites and nitrogen-doped carbon provided ORR active sites.[19] One concern about carbon material in oxygen electrolysis is that it is easily oxidized during OER process and thus

negatively affects the lifetime of the ZABs.[20] In addition, since carbon is a reducing agent while transition metal compounds are typically oxidants, side reaction may occur between the two components during the synthesis or operation process and will have an adverse influence on the electrode performance including both activity and stability.

Constructing a heterostructure from two or more transition compounds is an attractive strategy to develop bifunctional oxygen electrocatalysts which can avoid the potential carbon decomposition during the OER process.[20-22] As we all known, the catalytic activity of ORR and OER is determined by chemisorption rate of relevant species (OH^- and O_2 et.al.) on the surface of the electrocatalysts.[23] The creation of strong interactions between two different compounds through building heterostructure may promote the interfacial electron transport owning to modified electronic structure, which will accelerate the chemisorption of OH^- and O_2 for improving ORR and OER kinetics.[24-26] For example, it was reported by Qiao's group that the chemical coupling of CoO and Mn_3O_4 nano-octahedrons caused the formation of interfacial Mn-O-Co bonds and the appearance of high oxidation state of cobalt. The electron acceptor Mn_3O_4 nano-octahedrons drew the electrons from CoO, leading to the high-energy interfacial structure with active sites for ORR and OER. [25] Particularly, the heterostructural CuS/NiS_2, CoO/CoP, and NiO/CoN with interfacial interactions were also reported as bifunctional oxygen catalysts, and the interfacial atoms in these composites always played important role in enhanced catalytic performance.[27-29] To maximize this beneficial effect, developing a bifunctional catalyst with abundant atomic interface is favored, yet a great challenge.

Herein, for the first time, we reported a new Ru-based catalyst that show outstanding ORR and OER bifunctionality and superior durability. Sub-1 nm RuO_x clusters were grew on porous Co_3O_4 nanosheets by a smart surface precipitation strategy with only 4.1 *wt*% Ru loaded. High-energy interfacial Ru-O-Co bond was created between RuO_x cluster and the Co_3O_4 substrate,

thus altering the electronic structure of both RuO_x and Co_3O_4 to make the composite a superior electrocatalyst for both ORR and OER. The optimal RuO_x-nc@Co_3O_4-250 catalyst that was calcined at 250 ^oC exhibited ultralow potential gap (ΔE) of only 0.71 V between the potential of OER at 10 mA cm^{-2} (1.51 V) and the half-wave potential for ORR (0.80 V), much outperforming its counterpart based on the physical mixture of benchmark ORR/OER electrocatalysts of commercial Pt/C and nanosized RuO_2 (ΔE = 0.85 V). By using RuO_x-nc@Co_3O_4-250 as the air electrode in ZAB, remarkably, the cell delivered power density of 150 mW cm^{-2} at 300 mA cm^{-2}, superior durability for working over 250 h without obvious degradation, and excellent performance for the round-trip efficiency of 68.4% after 250 h test for rechargeable ZABs. Moreover, excellent rate performance up to 50 mA cm^{-2} was also observed. The fundamental understanding of the atomic high-energy interface formation and the outstanding catalytic performance is further exploited.

2. Results and discussion

2.1 Synthesis and characterization

The synthesis procedure of the bifunctional RuO_x-nc@Co_3O_4-250 catalyst is schematically depicted in **Figure 1a** and **Figure S1**. Here, layer-structured Co-LDH was first prepared by methanol-thermal process at 60 °C. Both the X-ray diffraction pattern (XRD) and scanning electron microscopy (SEM) images (**Figure S2)** confirmed nanosheet morphology of the obtained Co-LDH. Then, the yellow-colored Co-LDH was ultrasonically dispersed in deionized water to form a suspension, and $RuCl_3$ aqueous solution was subsequently added under magnetic stirring. Owing to the rich hydroxide (-OH) groups on the surface of Co-LDH nanosheets which could form complex with Ru^{3+}, Ru^{3+} was successfully homogeneously anchored on the surface of Co-LDH and the potential aggregation of Ru atoms was possibly avoided. The as-obtained dark grey $Ru(OH)_3$@Co-LDH precursor was then calcined at 150 – 450 °C in air for 3 h to obtain the black-colored composites, named as RuO_x-nc@Co_3O_4-T (T

= 150, 250, 350, and 450). For comparison, RuO_x-free Co_3O_4-250 was also prepared by the similar procedure but without step of adding $RuCl_3$ solution (calcined at 250 ^oC). The XRD patterns and SEM images of RuO_x-nc@Co_3O_4-T and Co_3O_4-250 as shown in **Figure S3** reveal the presence of crystal phase of $CoCo_2O_4$ (JCPDS 01-080-1533) and the similar 2D morphology of all catalysts.

The morphology and topography of the RuO_x-nc@Co_3O_4-250 were selected for further examination by atomic force microscopy (AFM). According to the SEM images as shown in **Figure 1b** and the AFM image in **Figure 1c**, the Co_3O_4 nanosheets have a thickness of ~3.6 nm (**Figure 1b, c**). Furthermore, the detailed porous feature and specific surface area of RuO_x-nc@Co_3O_4-250 and Co_3O_4-250 were explored by transmission electron microscopy (TEM) and nitrogen adsorption-desorption. According to the TEM images in **Figure 1d** (RuO_x-nc@Co_3O_4-250) and **Figure S4 (**Co_3O_4-250**)**, the mesoporous structure of nanosheets was well demonstrated. As shown in **Figure S5a**, both RuO_x-nc@Co_3O_4-250 and Co_3O_4-250 displayed type IV isotherms with hysteresis loop ($p/p_0 > 0.45$).[30] The corresponding specific pore size distribution (**Figure S5b**) indicates the mesoporous structure in nature (2–50 nm) of the catalysts, which is consistent with the TEM observation. Such mesopore-rich morphological structure enables the efficient transport of reaction species and easy contact with the electrolyte. In addition, RuO_x-nc@Co_3O_4-250 shows a high specific surface area of 115 $m^2\ g^{-1}$, which is higher than that of the Co_3O_4-250 catalyst (53 $m^2\ g^{-1}$), suggesting RuO_x contributed significantly to the surface area of RuO_x-nc@Co_3O_4-250 composite during synthesis process.

The XPS survey spectrum in **Figure S6** suggests the presence of cobalt, oxygen and ruthenium elements in sample RuO_x-nc@Co_3O_4-250, whereas the Co_3O_4-250 is mainly composed of cobalt and oxygen elements, as expected, suggesting the successful deposition of RuO_x on the surface of Co_3O_4 nanosheets in RuO_x-nc@Co_3O_4-250. However, from XRD pattern and TEM images, no any crystal phase of RuO_x was detected and no nanoparticles were

observed over the surface of Co_3O_4 nanosheets in RuO_x-nc@Co_3O_4-250. It suggests the RuO_x was likely homogeneously distributed and anchored on Co_3O_4-250 at atomic level. Such assumption was supported by the high angle annular dark field scanning transmission (HAADF-STEM) images as shown in **Figure 1e, 1f**, which clearly show many bright sub-nanometer RuO_x clusters (marked by orange circles) on the surface of Co_3O_4 nanosheets.[31, 32] Besides, a lattice spacing of ~0.287 nm corresponding to (220) plane of $CoCo_2O_4$ was observed in both RuO_x-nc@Co_3O_4-250 (**Figure S7**) and Co_3O_4-250 (**Figure S8a**) samples.[33] Furthermore, the elemental mapping of Co, O, and Ru was performed by the STEM energy dispersive X-ray spectrometry (STEM-EDX) (**Figure 1f)**, confirming again the RuO_x cluster supported on porous Co_3O_4 nanosheets in RuO_x-nc@Co_3O_4-250. In addition, the mass content of Ru in RuO_x-nc@Co_3O_4-250 was about 4.1% from the results of ICP test. Such low-load of Ru in RuO_x-nc@Co_3O_4-250 ensures that the prepared catalyst was cost-competitive. For comparison, the TEM-EDX elemental mapping images (**Figure S8b**) of Co_3O_4-250 just demonstrated uniform distribution of Co and O, while no Ru was detected. The RuO_x clusters can effectively adsorb hydroxyl and the mesoporous Co_3O_4 nanosheets with high surface area can adsorb molecular oxygen, thereby accelerating the kinetics of ORR and OER. In addition, owning to atomic dispersion of RuO_x and high surface area of Co_3O_4 substrate, extremely abundant interfaces between these two components were obtained, which may create an effect on the electronic structure of both phases, thus further tailoring the electrocatalytic performance.

2.2 Electrochemical performance

To evaluate the activity and bifunctionality for oxygen electrolysis, linear sweep voltammetry (LSV) was first used to explore the ORR and OER performance in the O_2-saturated 0.1 M KOH electrolyte at rotating speeds of 1600 rpm. Commercial state-of-the-art 20 wt. % Pt/C and nanosized RuO_2 particles (RuO_2-np) were served as the benchmark ORR and OER catalysts, respectively. In addition, the physical mixture of 20 wt. % Pt/C and RuO_2-

np (Pt/C+RuO_2-np) was also prepared to be used as contrastive bifunctional catalyst. To highlight the optimal calcination temperature and structural superiority of RuO_x-nc@Co_3O_4-250, several other catalysts were also prepared for comparison: (1) RuO_x-nc@Co_3O_4-T (T = 150, 350, and 450 °C), (2) Co_3O_4-250, (3) physical mixture of RuO_2-np and Co_3O_4-250 (RuO_2-np+Co_3O_4-250).

As shown in **Figure S9**, among the various catalysts, RuO_x-nc@Co_3O_4-250 delivered the highest catalytic activity for both ORR and OER. In addition, during ORR test, the limited current densities of the RuO_x-nc@Co_3O_4-T (T = 150, 250, 350, and 450 °C) catalysts were improved by increasing the rotating speed, demonstrating that the ORR was diffusion limited (**Figure S10**).[19] Then, the structural superiority of RuO_x-nc@Co_3O_4-250 was further explored. As shown in **Figure 2a**, RuO_x-nc@Co_3O_4-250 delivered the highest ORR catalytic activity with a limiting diffusion current of -6.2 mA cm^{-2} and half-wave potential of 0.80 V, compared with that of the Co_3O_4-250 (-4.5 mA cm^{-2}, 0.55 V), RuO_2-np (-4.7 mA cm^{-2}, 0.57 V), and RuO_2-np+Co_3O_4-250 (-4.9 mA cm^{-2}, 0.63 V), and even approached that of the commercial Pt/C (5.6 mA cm^{-2}, 0.82 V). Interestingly, the onset and half-wave potentials for the RuO_2-np+Co_3O_4-250 are also better than both RuO_2-np and Co_3O_4-250 in individual, implying there are also few contact interfaces between RuO_2-np and Co_3O_4-250 in the physically mixed composite. By depositing RuO_x clusters onto the surface of Co_3O_4 nanosheets, the as-derived RuO_x-nc@Co_3O_4-250 composite showed much superior ORR performance than the physically mixed RuO_2-np+Co_3O_4-250. As shown in **Figure S11**, Koutecky–Levich (K-L) equation was used to assess the ORR kinetics. The calculated electron transfer number for RuO_x-nc@Co_3O_4-250 and Pt/C is close to 4.0, indicating a four-electron reduction process. Meanwhile, **Figure 2b** shows the Tafel slope of 63 mV dec^{-1} for the RuO_x-nc@Co_3O_4-250, which is lower than Co_3O_4-250 (142 mV dec^{-1}), RuO_2-np (122 mV dec^{-1}), RuO_2-np+Co_3O_4-250 (79 mV dec^{-1}), further demonstrating the highest ORR activity in achieving high current at low potential.[25] The

catalytic durability of RuO_x-nc@Co_3O_4-250 and noble metal Pt/C for ORR were assessed by chronoamperometry measurements at 0.3 V.[34] As shown in **Figure 2c**, the RuO_x-nc@Co_3O_4-250 catalyst had the smallest deterioration rate of 8.7% after 10 h, which is obviously lower than the Pt/C catalyst (25.6%).

The OER electrocatalytic activity was further investigated to determine bifunctionality. Among these samples, RuO_x-nc@Co_3O_4-250 also achieved the highest OER catalytic activity with a small onset potential of 1.40 V and a low potential of 1.51 V at $E_{j=10\ mA\ cm^{-2}}$, which is obviously lower than that of Co_3O_4-250 (1.52, 1.65 V), RuO_2-np (1.42, 1.59 V), RuO_2-np+Co_3O_4-250 (1.42, 1.64 V). As regards to the commercial Pt/C, the inferior OER activity was observed contrary to its excellent ORR activity (**Figure 2d**). Moreover, RuO_x-nc@Co_3O_4-250 showed the smallest Tafel slope of 85 mV dec^{-1} compared to other catalysts, demonstrating the rate-determining step of OER is the surface chemical reaction process (**Figure 2e**). Also, the OER performance of RuO_x-nc@Co_3O_4-250 can assess by charge transfer impedance. The RuO_x-nc@Co_3O_4-250 showed the lowest charge transfer impedance from the EIS Nyquist plots at 1.56 V with amplitude of 5 mV in **Figure S12**, implying the best OER activity of the catalyst.[25] The catalytic durability of RuO_x-nc@Co_3O_4-250 and RuO_2-np for OER were assessed by chronopotentiometry measurements at 10 mA cm^{-2}.[34] As shown in **Figure 2f**, the RuO_x-nc@Co_3O_4-250 catalyst showed slight increase of 45 mV in potential over 12 h test, while the RuO_2-np exhibited a rapid loss of OER activity within 2 h.

The bifunctionality performance of the oxygen electrocatalysts was confirmed by potential gap (ΔE) between the potential of OER at 10 mA cm^{-2} and the half-wave potential for ORR. As shown in **Figure 2g**, the RuO_x-nc@Co_3O_4-250 exhibited the lowest ΔE of 0.71 V among the comparative catalysts, implying the RuO_x clusters in RuO_x-nc@Co_3O_4-250 played an important role in improving both the electrocatalytic activity of ORR and OER. More importantly, the bifunctional performance of RuO_x-nc@Co_3O_4-250 was also compared with

physical mixture of commercial noble metal catalysts Pt/C and RuO_2-np (Pt/C+RuO_2-np) with the ΔE of 0.85 V, showing the superior bifunctional electrocatalytic activity of RuO_x-nc@Co_3O_4-250 (**Figure 2h**). To highlight the superior bifunctionality of our catalyst, a comparison with recently reported cobalt-based electrocatalysts was also executed in **Figure 2i** (detail information shown in **Table S1**), which clearly demonstrates the superior bifunctional activity of our work.

The practical application of the designed RuO_x-nc@Co_3O_4-250 bifunctional catalyst in ZABs was then exploited. The ZAB was assembled with the bifunctional catalyst as air cathode, zinc plate as the anode, and 6.0 M KOH + 0.2 M $ZnCl_2$ as the electrolyte (**Figure 3a**). For comparison, a similar cell with the physically mixed benchmark Pt/C+RuO_2-np composite electrocatalyst as the air electrode was also fabricated and tested. As shown in **Figure S13**, the ZAB with the RuO_x-nc@Co_3O_4-250 air electrode showed open circuit voltage (OCV) of 1.455 V, higher than that of the cell with the Pt/C+RuO_2-np air electrode (1.345 V). The polarization curves of the ZAB with the RuO_x-nc@Co_3O_4-250 air electrode showed a higher reduction current density than that of the ZAB with the Pt/C+RuO_2-np air electrode, which is probably due to higher ORR limiting current of RuO_x-nc@Co_3O_4-250. Moreover, the ZAB with RuO_x-nc@Co_3O_4-250 air electrode showed attractive power density of 150 mW cm^{-2} at 300 mA cm^{-2}, which is slightly higher than the cell with the ZAB with Pt/C+RuO_2-np air electrode (143 mW cm^{-2}, **Figure 3b**). Furthermore, the ZAB with RuO_x-nc@Co_3O_4-250 showed remarkably smaller charge-discharge voltage gap than that of the cell with Pt/C+RuO_2-np air electrode (**Figure 3c**), agreeing well with the results of ORR and OER test (**Figure 2h**).

The durability of the bifunctional catalysts in ZABs was also evaluated by galvanostatic charge-discharge test. By cycling at 2 mA cm^{-2} (**Figure 3d and Figure S14**), the ZABs with the RuO_x-nc@Co_3O_4-250 air electrode showed an initial charge/discharge polarization potential of 0.52 V, obviously lower than of the cell with the Pt/C+RuO_2-np air electrode with

0.64 V. It increased to 0.61 V for the RuO_x-nc@Co_3O_4-250 catalyst after cycled for 250 h. As a comparison, it increased to 0.96 V for Pt/C+RuO_2-np after 150 h. More importantly, RuO_x-nc@Co_3O_4-250 air electrode showed a high round-trip efficiency of 68.4% after 250 h, while the Pt/C+RuO_2-np is 55.4% after 150 h (**Figure 3e**). The cycling performance and energy efficiency of the cell with RuO_x-nc@Co_3O_4-250 electrode is also better than recently reported work (**Table S2**). In addition, from the photograph of the ZABs after cycled for 250 h as shown in **Figure S15**, the collected electrolyte remained transparent and colorless as fresh electrolyte, manifesting the excellent structural stability of the RuO_x-nc@Co_3O_4-250 catalyst.[20] In contrast, the electrolyte turn to brown after charge/discharge test for the battery with carbon cloth cathode.

The rate performance of bifunctional catalysts was further explored. As shown in **Figure 3f**, the ZAB with the RuO_x-nc@Co_3O_4-250 air electrode achieved round-trip efficiency of 69.3%, 65.1%, 61.1%, and 50.0% at current densities of 5, 10, 20, and 50 mA cm^{-2}, respectively. When the current density was returned to 5 mA cm^{-2}, a stable discharge/charge curve for 500 cycles was still obtained, as shown in **Figure 3g**, indicating a good rate stability of the RuO_x-nc@Co_3O_4-250 catalyst. For comparison, the cell with the benchmark Pt/C+RuO_2-np composite catalyst showed round-trip efficiency of 65.6%, 58.5%, 52.9%, and 42.0% at current densities of 5, 10, 20, and 50 mA cm^{-2}, respectively (**Figure S16**). Then, the cycling performance at high current density of 20 mA cm^{-2} was further evaluated with the results shown in **Figure 3h and Figure S17** for the ZABs with RuO_x-nc@Co_3O_4-250 and Pt/C+RuO_2-np air electrodes, respectively. The initial charge/discharge polarization of the ZAB with RuO_x-nc@Co_3O_4-250 air electrode reached 0.80 V (0.97 V for ZAB with Pt/C+RuO_2-np air electrode), and the final values is 0.92 V after 80 h test (1.65 V for ZAB with Pt/C+RuO_2-np air electrode after 20 h test). Therefore, the RuO_x-nc@Co_3O_4-250-based rechargeable ZAB showed excellent cycling stability and rate performance, outperforming its counterpart based

on Pt/C+RuO_2-np air-cathode and most other reported bifunctional catalysts (**Table S2**). Finally, we also use three series-wound ZABs to power a big (F**igure 3i**) and small (**Figure S18**) LED viewing screen for 10 and 48 h, respectively, demonstrating that the ZABs with RuO_x-nc@Co_3O_4-250 air-electrode can be applied in various practical power devices. Hence, these results of ZABs strongly prove that the RuO_x-nc@Co_3O_4-250 can serve as an efficient ORR and OER bifunctional electrocatalyst for practical application in real electrochemical device.

2.3 Origins of bifunctional activity

To exploit the origin of the superior bifunctionality for the RuO_x-nc@Co_3O_4 catalyst, the chemical interaction between RuO_x cluster and porous Co_3O_4 nanosheets was first detected by Raman spectroscopy. Raman spectra of RuO_x-nc@Co_3O_4-250, Co_3O_4-250 and RuO_2 nanoparticles (RuO_2-np) are shown in **Figure 4a**. Three typical characteristic Raman peaks of Co_3O_4-250, located at 191, 471, and 671 cm^{-1}, were observed, which can be assigned to F_{2g}, E_g, and A_{1g} modes of Co-O bond, respectively.[16, 35] For RuO_2-np, two main characteristic peaks located at 505 and 622 cm^{-1}, corresponding to E_g and A_{1g} modes of Ru-O bond, were observed.[36] Surprisingly, for the RuO_x-nc@Co_3O_4-250 sample, redshift of A_{1g} mode compared to Co_3O_4-250 was observed. In addition, the asymmetric A_{1g} mode was also observed for the RuO_x-nc@Co_3O_4-250 sample. Therefore, the detailed fitted A_{1g} spectra of the three samples were further revealed in **Figure 4b**. The A_{1g} spectrum of RuO_x-nc@Co_3O_4-250 can be deconvoluted into two peaks located at 671 and 657 cm^{-1}, which can be assigned to stretching vibration of Co-O and Ru-O bond, respectively. The redshift of A_{1g} modes of Co-O (671 cm^{-1} to 657 cm^{-1}) and the blueshift of A_{1g} modes (622 cm^{-1} to 657 cm^{-1}) illustrates the RuO_x clusters can affect the stretching vibration of Co-O bond and Co_3O_4 can also affect the stretching vibration of Ru-O bond, implying the formation of Ru-O-Co bond on the interface of RuO_x clusters and Co_3O_4 nanosheets.[25,37] Furthermore, for RuO_x-nc@Co_3O_4-250, the disappearance

of E_g modes of Ru-O bond implies RuO_x was distributed in atomic level, which is consistent with previous discussion. In addition, the energy band gap of RuO_x-nc@Co_3O_4-250 is determined to be 1.70 eV, which is lower than 1.88 eV for Co_3O_4-250, it means the conductivity of RuO_x-nc@Co_3O_4-250 was improved as compared to Co_3O_4-250 (**Figure S19**). These results suggest the appearance of strong electronic interaction between RuO_x clusters and Co_3O_4 nanosheets in the composite with the formation of Ru-O-Co bond at interface, and such interaction also resulted in improved conductivity of RuO_x-nc@Co_3O_4-250, thus accelerating the electron charge transfer during ORR and OER processes.

To get further insights into origin of bifunctional activity for RuO_x-nc@Co_3O_4-250, X-ray photoelectron spectroscopy (XPS) measurements were performed to explore the relationship between interfacial Ru-O-Co bond and bifunctional activity. In the high-resolution Ru 3p XPS spectrum of RuO_x-nc@Co_3O_4-250 (**Figure 4c**), the peaks located at 463.6 and 485.8 eV are ascribed to Ru^{3+} $3p_{3/2}$ and Ru^{3+} $3p_{1/2}$, respectively, indicating the Ru in RuO_x-nc@Co_3O_4-250 is almost the unsaturated trivalent Ru atoms.[10] Differently, the Ru 3p XPS spectrum of RuO_2-np (**Figure 4e**) shows the coexistence of Ru^{3+} (462.3 and 484.7 eV) and Ru^{4+} (465.4 and 487.8 eV).[38-40] Obvious positive shift of 1.3 eV for Ru^{3+} in RuO_x-nc@Co_3O_4-250 was observed as compared to RuO_2-np, suggesting the Ru^{3+} in RuO_x-nc@Co_3O_4-250 can serve as an electron donor owning to the influence of the Co_3O_4 supporter.[25, 40] More importantly, the electron deficient Ru^{3+} can serve as the host to anchor the OH^- in the electrolyte. Considering the charge balance, the Co_3O_4 substrate will obtain the electron flowing form RuO_x clusters. Then, the Co 2p XPS spectrums of RuO_x-nc@Co_3O_4-250 and Co_3O_4-250 were further explored. As shown in **Figure S20a**, the high-resolution Co $2p_{3/2}$ XPS spectrum of RuO_x-nc@Co_3O_4-250 showed the coexistence of Co^{3+} (779.5 eV) and Co^{2+} (780.9 and 782.3 eV).[41-43] The Co $2p_{3/2}$ XPS spectrum of Co_3O_4-250 also exhibited the coexistence of Co^{3+} and Co^{2+} (**Figure S20b**). Surprisingly, the peaks of Co^{2+} in RuO_x-nc@Co_3O_4-250 negatively shifted about 0.4 eV as

compared to the peaks of Co^{2+} in Co_3O_4-250, implying the strong electronic interaction between RuO_x clusters and Co_3O_4 substrate. Hence, the electron-rich Co site in RuO_x-nc@Co_3O_4-250 can serve as host for anchoring the oxygen during the ORR process. The detailed Co-O and Ru-O bonds were further explored by O 2p XPS spectrum. As shown in **Figure 4d, 4f**, the O 1s spectrum in RuO_x-nc@Co_3O_4-250 and Co_3O_4-250 showed two peaks located at 529.7, and 530.9 eV, attributed to Co-O and Co-OH, respectively.[43] Interestingly, the O 1s spectrum in RuO_x-nc@Co_3O_4-250 showed two additional peaks, located at 532.0 and 533.1 eV, corresponding to the Ru-O-Co and Ru-OH band, respectively.[39] Compared to the O 1s spectrum of RuO_2-np (**Figure S21**), the obvious positive shift of ~3 eV for RuO_x-nc@Co_3O_4-250 can further confirm that the RuO_x clusters were anchored on Co_3O_4 nanosheets through the formation of high-energy interfacial chemical bond,[25] i.e., the Ru-O-Co bond at the interface of RuO_x clusters and Co_3O_4 nanosheets.

The effect of high-energy interfacial Co-O-Ru bond in ORR and OER activity was further investigated. For better understanding of the ORR/OER mechanism, XPS measurements of RuO_x-nc@Co_3O_4-250 catalyst after 100 cycles at 10 mA cm^{-2} (RuO_x-nc@Co_3O_4-250 after 100 cycles) was conducted. The corresponding cycling performance of ZAB is shown in **Figure S22**. In the high-resolution Ru 3p XPS spectrum of RuO_x-nc@Co_3O_4-250 after 100 cycles (**Figure 4g**), two peaks located at Ru^{3+} $3p_{3/2}$ and Ru^{3+} $3p_{1/2}$ were also observed, in accordance with Ru 3p spectrum of RuO_x-nc@Co_3O_4-250 without any shift of binding energy or other valence of Ru, implying the superior stability of RuO_x clusters. The additional peak at 474.5 eV was attributed to the Zn Auger, resulting from the electrolyte. As shown in **Figure S20c**, the high-resolution Co $2p_{3/2}$ XPS spectrum of RuO_x-nc@Co_3O_4-250 after 100 cycles also reveals similar results for the coexistence of Co^{3+} and Co^{2+}. These results reveal that the electronic structure of RuO_x-nc@Co_3O_4-250 remained the original status after 100 cycles at 10 mA cm^{-2}, further demonstrating the excellent structural stability of bifunctional catalysts RuO_x-

nc@Co_3O_4-250. Then O 1s XPS spectrum of RuO_x-nc@Co_3O_4-250 after 100 cycles was further explored. As shown in **Figure 4h**, the four peaks of Co-O, Co-OH, Ru-O-Co, and Ru-OH were also observed without any shift compared to that of fresh RuO_x-nc@Co_3O_4-250. In addition, an emerging peak at 535.6 eV was attributed to adsorbed H_2O*,[44] and the relative intensity of Ru-O-Co and Ru-OH bond was obviously changed, which was caused by adsorption/desorption of H_2O*/OH* during ORR and OER process.

As shown in **Figure 5a**, obvious anodic and cathodic peaks for Co_3O_4-250 are observed from the CV curves, corresponding to the redox reactions between Co^{3+} and Co^{4+} in alkaline solutions. Previous work reveals that the charge-transfer process is the common characteristic of Co_3O_4 catalyst.[45, 46] In comparison, the RuO_x-nc@Co_3O_4-250 catalyst shows no anodic and cathodic peaks corresponding to the redox reactions between Co^{3+} and Co^{4+}, revealing that the Co_3O_4 supporter are not active site during oxidation and reduction processes for the RuO_x-nc@Co_3O_4-250 catalyst. In addition, the values of Co^{3+}/Co^{2+}, Co-O/Co-OH, and Ru-O-Co/Ru-OH are then compared in **Figure 5b**. The similar values of Co^{3+}/Co^{2+} for the RuO_x-nc@Co_3O_4-250, RuO_x-nc@Co_3O_4-250 after 100 cycles, and Co_3O_4-250 were observed, implying the same surface structure of the Co_3O_4-250 supporter before and after cycling. For the ratio of Co-O/Co-OH, both samples of RuO_x-nc@Co_3O_4-250 and RuO_x-nc@Co_3O_4-250 after 100 cycles showed the same values, demonstrating the Co-O is not the active site for adsorption of OH* during ORR and OER. Compared to Co_3O_4-250, the lower value of Co-O/Co-OH was mainly caused by the coverage of RuO_x clusters on the surface of Co_3O_4 nanosheets. Interestingly, the values of Ru-O-Co/Ru-OH for RuO_x-nc@Co_3O_4-250 (2.73) were obviously larger than RuO_x-nc@Co_3O_4-250 after 100 cycles (1.08), implying the content of Ru-OH bond was largely improved after the ZABs test. These results reveal that the Ru^{3+} are the main active sites for adsorption of OH* during ORR and OER processes. As the results of XPS, the RuO_x clusters were anchored on porous Co_3O_4 nanosheets by the formation of high-energy interfacial Ru-O-

Co bond. Therefore, the loaded RuO_x clusters are the main reactive site during ORR/OER processes. As shown in **Figure 5c**, because of the unsaturated Ru^{3+} natures of the high-energy interfacial Ru-O-Co bond, adsorptions of relevant species (O*, OH*, OO*, and OOH*) was appeared to compensate its four-fold coordination to form Ru-centered tetrahedral crystal fields.[47] Based on the abovementioned analysis, the excellent performance of ORR/OER and Zn-air batteries are attributed to unique high-energy interfacial Ru-O-Co bonds between RuO_x clusters and porous Co_3O_4 nanosheets. The proposed mechanism for the RuO_x-nc@Co_3O_4-250 catalyst was schematic illustrated in **Figure 5d**. During OER process, the high-energy unsaturated Ru^{3+} is easy to adsorb OH^- from electrolyte, thus markedly improving the OER performance. As for ORR process, the electron-rich mesoporous Co_3O_4 nanosheets, with high specific surface area of 115 $m^2\ g^{-1}$, can anchor the oxygen molecule from the electrolyte. Then, the adsorbed O_2* on Co_3O_4 surface can transfer to the reactive site of unsaturated Ru^{3+} by the Co-O-Ru bond, thus collaboratively improve the performance of both ORR and OER. Furthermore, the RuO_x-nc@Co_3O_4-250 catalyst showed the superior stability toward ORR and OER compared with Pt/C and RuO_2-np, also implying the formation of Ru-O-Co bond between RuO_x clusters and Co_3O_4 nanosheets can effectively avoid the dissolution of RuO_2 in the alkaline electrolyte, thus improving the structure stability of RuO_x cluster.

3. Conclusions

In summary, we have synthesized RuO_x sub-1 nm clusters on porous Co_3O_4 nanosheets via a facile two-step process involving a surface precipitation and thermal treatment. Owning to the formation of abundant high-energy interfacial Ru-O-Co bonds, the strong electronic interaction between RuO_x clusters and Co_3O_4 porous nanosheets significantly improved the ORR and OER kinetics and structural stability of RuO_x clusters. An ultralow potential gap (ΔE) of 0.71 V between the potential of OER at 10 mA cm^{-2} (1.51 V) and the half-wave potential for ORR (0.80 V) (ΔE = 0.71 V) was obtained for the as-prepared RuO_x-nc@Co_3O_4-250

catalyst, which largely outperformed its counterpart based on physical mixture of Pt/C+RuO_2-np air-cathode (ΔE = 0.85 V) and other available bifunctional electrocatalysts as reported in literatures. Such superiority was due to the creation of atomic high-energy interface Ru-O-Co bond, which caused a change in electronic structure for both Ru and Co, and then introducing beneficial effect for reaction intermediate adsorption/desorption. As well, the formation of high-energy Ru-O-Co bond between RuO_x and Co_3O_4 at atomic level suppressed the dissolution of RuO_2 into liquid electrolyte, resulting in improved durability of the catalyst. In rechargeable ZABs, RuO_x-nc@Co_3O_4-250-based air electrode showed superior durability for working over 250 h and excellent performance for the round-trip efficiency of 68.4% even after 250 h. Moreover, the excellent rate performance up to 50 mA cm^{-2} was also observed for RuO_x-nc@Co_3O_4-250-based electrode. Hence, the RuO_x-nc@Co_3O_4-250 electrocatalyst exhibits a significant breakthrough in the development of practical ZABs. This work presents a simple strategy to design cost-competitive Ru-based electrocatalyst with superior bifunctionality for rechargeable ZABs, hence encouraging more research studies on fabrication of other metallic oxide compounds as bifunctional electrocatalysts for energy conversion/storage.

4. Experimental section

4.1 Synthesis of RuO_x@Co_3O_4-250

Co-LDH was first prepared by methanol-thermal process. Briefly, 0.65 g $Co(NO_3)_2 \cdot 6H_2O$ and 1.35 g hexamethylenetetramine were dissolved in 10 mL methanol at room temperature, respectively. Then, the Co(II) solution was slowly poured into hexamethylenetetramine solution under magnetic stirring for 5 min, and the obtained red solution was further continued stirred at 60 °C for 6 h. Thereafter, the yellow powder was collected through vacuum filtration, washed with methanol for several times, and finally dried in oven at 60 °C for 5 h to obtain the Co-LDH powder.

For the synthesis of $RuO_x@Co_3O_4$-250, 80 mg Co-LDH powder was first ultrasonically dispersed in 50 mL deionized water for 10 min, and then, 250 μL 20 mg mL^{-1} $RuCl_3$ solution was added into the Co-LDH solution under magnetic stirring for 5 h. Subsequently, the suspended powder was collected through vacuum filtration, washing with water and ethanol for several times, and dried in oven at 60 °C for 2 h. Finally, the obtained powder was annealing at 250 °C (150 °C, 350 °C, and 450 °C) with heating rate of 5 °C min^{-1} for 3 h in muffle furnace. In the control experiment, Co_3O_4-250 was also prepared as same as the $RuO_x@Co_3O_4$-250 except for adding the $RuCl_3$ solution.

4.2 Material characterization

Powder X-ray diffraction (PXRD) patterns were conducted on Rigaku Smart Lab (Cu Kα radiation, λ = 1.5406 Å, 40 kV and 40 mA). The morphologies and microstructure of catalysts were obtained by scanning electron microscope (SEM, Hitachi S-4800), high-resolution transmission electron microscope (HRTEM, TM3000), and high angle annular dark field scanning transmission (HAADF-STEM, FEI Titan Cubed Themis G2 300). In addition, nitrogen adsorption-desorption isotherms were collected by BELSORP II instrument at 77 K, and the corresponding specific surface areas and pore size distributions were acquired by Brunauer-Emmett-Teller (BET) equation and Barrett-Joyner-Halenda (BJH) method, respectively. Raman spectra of the catalysts were conducted at a Horiba LabRAM HR spectroscope with excitation laser of 632 nm. X-ray photoelectron spectroscopy spectrometer were collected on PHI5000 Versa Probe with an Al Kα X-ray source, and all the data are corrected with C 1s line as 284.6 eV. UV–vis spectra was conducted at Lambda 750 S within wavelength of 400 – 900 nm.

4.3 Electrochemical tests

The ORR and OER performance of these catalysts were recorded at potentiostation (CHI 760e) with a rotation speed controller (Pine Instrument Co.) by a standard three-electrode electrolytic cell. 10 mg of RuO_x@Co_3O_4-250 (5 mg Pt/C and 5 mg RuO_2-np) and 5 mg acetylene black were added into mixed solution of isopropanol and Nafion (5%) (volume ratio of 9: 1) to form a homogeneous catalyst ink with the catalyst concentration of 10 mg mL^{-1}. Then, 5 μL prepared ink was dropped onto a clean glassy carbon electrode (GCE) surface via pipette and further dried in air for 30 min with the catalyst load of 0.25 mg cm^{-2}, and the obtained glassy carbon electrode serve as work electrode. The Hg/HgO (1 M KOH) and carbon rod were served as reference and counter electrodes, respectively. The ORR and OER performance were all recorded in the O_2-saturated 0.1 M KOH solution at rotation speed of 1600 rpm.

Linear sweep voltammetry (LSV) of ORR was executed at a scan rate of 5 mV s^{-1} within 0.2 - 0.7 V versus Hg/HgO. The LSV profiles of ORR at different rotation speeds (400, 800, 1200, 1600, 2000, and 2500 rpm) were also measured. The electron transfer number of these catalysts were calculated by Koutecky–Levich equation as:

$$j^{-1} = j_k^{-1} + j_L^{-1}$$

$$j_k = nFkC_{O_2}$$

$$j_L = 0.62nFD_{O_2}^{2/3}v^{-1/6}C_{O_2}\omega^{1/2}$$

Where n, F, C_{O2}, D_{O2}, υ, and ω is transferred electron number, Faraday constant, the concentration of O_2 in the electrolyte, the diffusion coefficient of O_2 in 0.1 M KOH, the kinematic viscosity, and the angular velocity (rpm), respectively.

LSV profile of OER was executed at potential within 0.2 - 1.1 V versus Hg/HgO with a scan rate of 5 mV s^{-1}. The potentials were corrected to RHE scale via calibrated equation as:

$$E_{RHE} = E_{Hg/HgO} + 0.059pH + 0.098$$

The durability of RuO_x@Co_3O_4-250 was conducted at a constant potential of 0.30 V (vs RHE) for the ORR and at a constant current density of 10 mA cm^{-2} for the OER.

4.4 Fabrication of Zn-air batteries

The home-made Zn-Air batteries were assembled with the catalysts loaded on gas diffusion layer as air electrode, a Zn foil as the metal electrode, and 6 M KOH + 0.2 M $ZnCl_2$ aqueous solution as the electrolyte. Typically, RuO_x@Co_3O_4-250 and acetylene black (mass ratio of 2: 1) were dispersed in mixed solution of isopropanol and 5% Nafion (volume ratio of 9: 1) solution with the concentration of 10 mg mL^{-1} for the catalyst, and the obtained catalyst ink was then drop-cast onto one face of gas diffusion layer as air electrode, guaranteeing a mass loading of 2 mg cm^{-2}. For comparison, the mixture of Pt/C and RuO_2-np with mass ratio of 1: 1 was also prepared as RuO_x@Co_3O_4-250, and then drop-cast onto one face of gas diffusion layer with mass loading of 2 mg cm^{-2}.

4.5 Performance evaluation of Zn-air batteries

All the tests were conducted at ambient atmosphere and temperature. The discharge/charge polarization curves (voltage-current) were conducted at CHI 760e at a voltage step of 0.5 mV s^{-1}. The galvanostatic charge/discharge curves were collected by the LAND CT2001A testing system. The big LED screen and small LED screen (> 3 V) are home-made and commercially available, respectively.

Appendix A. Supplementary material

Supplementary data associated with this article can be found in the online version at XXX.

Declarations of interest:

The authors declare no competing financial interest.

Acknowledgements

This work was financially supported by National Natural Science Foundation of China (No. 51802152), National Key R&D Program of China (No. 2018YFB0905400), Natural Science Foundation of Jiangsu Province of China (No. BK20170974), and Priority Academic Program Development of Jiangsu Higher Education Institutions.

References

[1] S. Chu, Y. Cui, N. Liu, Nat. Mater., 16 (2016) 16-22.

[2] K. Liao, S. Wu, X. Mu, Q. Lu, M. Han, P. He, Z. Shao, H. Zhou, Adv. Mater., 30 (2018) 1705711.

[3] X. Zou, K. Liao, D. Wang, Q. Lu, C. Zhou, P. He, R. Ran, W. Zhou, W. Jin, Z. Shao, Energy Storage Mater., 27 (2020) 297-306.

[4] M. Du, K. Liao, Q. Lu, Z. Shao, Energy Environ. Sci., 12 (2019) 1780-1804.

[5] J. S. Lee, S. T. Kim, R. Cao, N. S. Choi, M. Liu, K. T. Lee, J. Cho, Adv. Energy Mater., 1 (2011) 34-50.

[6] Y. Li, H. Dai, Chem. Soc. Rev., 43 (2014) 5257-5275.

[7] J. Yi, P. Liang, X. Liu, K. Wu, Y. Liu, Y. Wang, Y. Xia, J. Zhang, Energy Environ. Sci., 11 (2018) 3075-3095.

[8] X. Zou, Q. Lu, Y. Zhong, K. Liao, W. Zhou, Z. Shao, Small, 14 (2018) e1801798.

[9] J. Fu, Z.P. Cano, M.G. Park, A. Yu, M. Fowler, Z. Chen, Adv. Mater., 29 (2017) 1604685.

[10] X. Meng, K. Liao, J. Dai, X. Zou, S. She, W. Zhou, F. Ye, Z. Shao, ACS Appl. Mater. Interfaces., 11 (2019) 20091-20097.

[11] J. Yu, Y. Guo, S. She, S. Miao, M. Ni, W. Zhou, M. Liu, Z. Shao, Adv. Mater., 30 (2018) 1800047.

[12] B. J. Kim, D.F. Abbott, X. Cheng, E. Fabbri, M. Nachtegaal, F. Bozza, I.E. Castelli, D. Lebedev, R. Schäublin, C. Copéret, T. Graule, N. Marzari, T.J. Schmidt, ACS Catal., 7 (2017) 3245-3256.

[13] Y. Yao, S. Hu, W. Chen, Z. Q. Huang, W. Wei, T. Yao, R. Liu, K. Zang, X. Wang, G. Wu, W. Yuan, T. Yuan, B. Zhu, W. Liu, Z. Li, D. He, Z. Xue, Y. Wang, X. Zheng, J. Dong, C.-R. Chang, Y. Chen, X. Hong, J. Luo, S. Wei, W.-X. Li, P. Strasser, Y. Wu, Y. Li, Nat. Catal., 2 (2019) 304-313.

[14] S.H. Chang, N. Danilovic, K.C. Chang, R. Subbaraman, A.P. Paulikas, D.D. Fong, M.J. Highland, P.M. Baldo, V.R. Stamenkovic, J.W. Freeland, J.A. Eastman, N.M. Markovic, Nat. Commun., 5 (2014) 4191.

[15] X. Han, X. Wu, C. Zhong, Y. Deng, N. Zhao, W. Hu, Nano Energy, 31 (2017) 541-550.

[16] G. Fu, J. Wang, Y. Chen, Y. Liu, Y. Tang, J.B. Goodenough, J.-M. Lee, Adv. Energy Mater., 8 (2018) 1802263.

[17] W. Niu, Z. Li, K. Marcus, L. Zhou, Y. Li, R. Ye, K. Liang, Y. Yang, Adv. Energy Mater., 8 (2018) 1701642.

[18] Y. Qiao, P. Yuan, Y. Hu, J. Zhang, S. Mu, J. Zhou, H. Li, H. Xia, J. He, Q. Xu, Adv. Mater., 30 (2018) e1804504.

[19] Q. Lu, J. Yu, X. Zou, K. Liao, P. Tan, W. Zhou, M. Ni, Z. Shao, Adv. Funct. Mater., 29 (2019) 1904481.

[20] S. Song, W. Li, Y.-P. Deng, Y. Ruan, Y. Zhang, X. Qin, Z. Chen, Nano Energy, 67 (2020) 104208.

[21] G.-P. Kim, H.-H. Sun, A. Manthiram, Nano Energy, 30 (2016) 130-137.

[22] J. Diao, Y. Qiu, S. Liu, W. Wang, K. Chen, H. Li, W. Yuan, Y. Qu, X. Guo, Adv. Mater., (2019) 1905679.

[23] X. R. Wang, J. Y. Liu, Z. W. Liu, W. C. Wang, J. Luo, X. P. Han, X. W. Du, S. Z. Qiao, J. Yang, Adv. Mater., 30 (2018) 1800005.

[24] X.F. Lu, Y. Chen, S. Wang, S. Gao, X.W.D. Lou, Adv. Mater., 31 (2019) e1902339.

[25] C. Guo, Y. Zheng, J. Ran, F. Xie, M. Jaroniec, S.Z. Qiao, Angew. Chem., Int. Ed., 56 (2017) 8539-8543.

[26] T. Hu, Y. Wang, L. Zhang, T. Tang, H. Xiao, W. Chen, M. Zhao, J. Jia, H. Zhu, Appl. Catal., B: Environ., 243 (2019) 175-182.

[27] L. An, Y. Li, M. Luo, J. Yin, Y.-Q. Zhao, C. Xu, F. Cheng, Y. Yang, P. Xi, S. Guo, Adv. Funct. Mater., 27 (2017) 1703779.

[28] W. Jin, J. Chen, B. Liu, J. Hu, Z. Wu, W. Cai, G. Fu, Small, 15 (2019) 1904210.

[29] J. Yin, Y. Li, F. Lv, Q. Fan, Y.Q. Zhao, Q. Zhang, W. Wang, F. Cheng, P. Xi, S. Guo, ACS Nano, 11 (2017) 2275-2283.

[30] Q. Lu, Y. Zhong, W. Zhou, K. Liao, Z. Shao, Adv. Mater. Interfaces, 5 (2018) 1701659.

[31] L. Liu, A. Corma, Chem. Rev., 118 (2018) 4981-5079.
[32] L. Howard-Fabretto, G. G. Andersson, Adv. Mater., (2019) 1904122. https://doi.org/10.1002/adma.201904122.
[33] T. Wu, S. Sun, J. Song, S. Xi, Y. Du, B. Chen, W.A. Sasangka, H. Liao, C.L. Gan, G.G. Scherer, L. Zeng, H. Wang, H. Li, A. Grimaud, Z.J. Xu, Nat. Catal., 2 (2019) 763-772.
[34] X.T. Wang, T. Ouyang, L. Wang, J.H. Zhong, T. Ma, Z.Q. Liu, Angew. Chem., Int. Ed., 58 (2019) 13291-13296.
[35] Z. Guo, F. Wang, Y. Xia, J. Li, A.G. Tamirat, Y. Liu, L. Wang, Y. Wang, Y. Xia, J. Mater. Chem. A, 6 (2018) 1443-1453.
[36] H. Su Jang, Y. Yang, N.-S. Lee, B. Son, Y. Lee, C. Lee, M. Hwa Kim, Mater. Lett., 139 (2015) 405-408.
[37] Y. Liu, N. Fu, G. Zhang, M. Xu, W. Lu, L. Zhou, H. Huang, Adv. Funct. Mater., 27 (2017) 1605307.
[38] S. Zhai, C. Wang, H.E. Karahan, Y. Wang, X. Chen, X. Sui, Q. Huang, X. Liao, X. Wang, Y. Chen, Small, 14 (2018) 1800582.
[39] H. Li, X. Li, J. Liang, Y. Chen, Adv. Energy Mater., 9 (2019) 1803987.
[40] Q. Lu, Y. Sun, K. Liao, X. Zou, I. Hamada, W. Zhou, M. Ni, Z. Shao, Electrochim. Acta, 298 (2019) 421-429.
[41] X. Xu, Z. Zhong, X. Yan, L. Kang, J. Yao, J. Mater. Chem. A, 6 (2018) 5999-6006.
[42] H. Liang, F. Meng, M. Caban-Acevedo, L. Li, A. Forticaux, L. Xiu, Z. Wang, S. Jin, Nano Lett., 15 (2015) 1421-1427.
[43] J. Yang, H. Liu, W.N. Martens, R.L. Frost, J. Phys. Chem. C, 114 (2010) 111-119.
[44] X. Wang, J. Sunarso, Q. Lu, Z. Zhou, J. Dai, D. Guan, W. Zhou, Z. Shao, Adv. Energy Mater., 10 (2019) 1903271.
[45] Peng Tan, Bin Chen, Haoran Xu, Weizi Cai, Wei He, Meng Ni, Appl. Catal., B: Environ., 241 (2019) 104-112.
[46] Peng Tan, Bin Chen, Haoran Xu, Weizi Cai, Wei He, Meilin Liu, Zongping Shao, Meng Ni, Small, 14 (2018) 1800225.
[47] J. Suntivich, H.A. Gasteiger, N. Yabuuchi, H. Nakanishi, J.B. Goodenough, Y. Shao-Horn, Nat. Chem., 3 (2011) 546-550.

Figures and captions

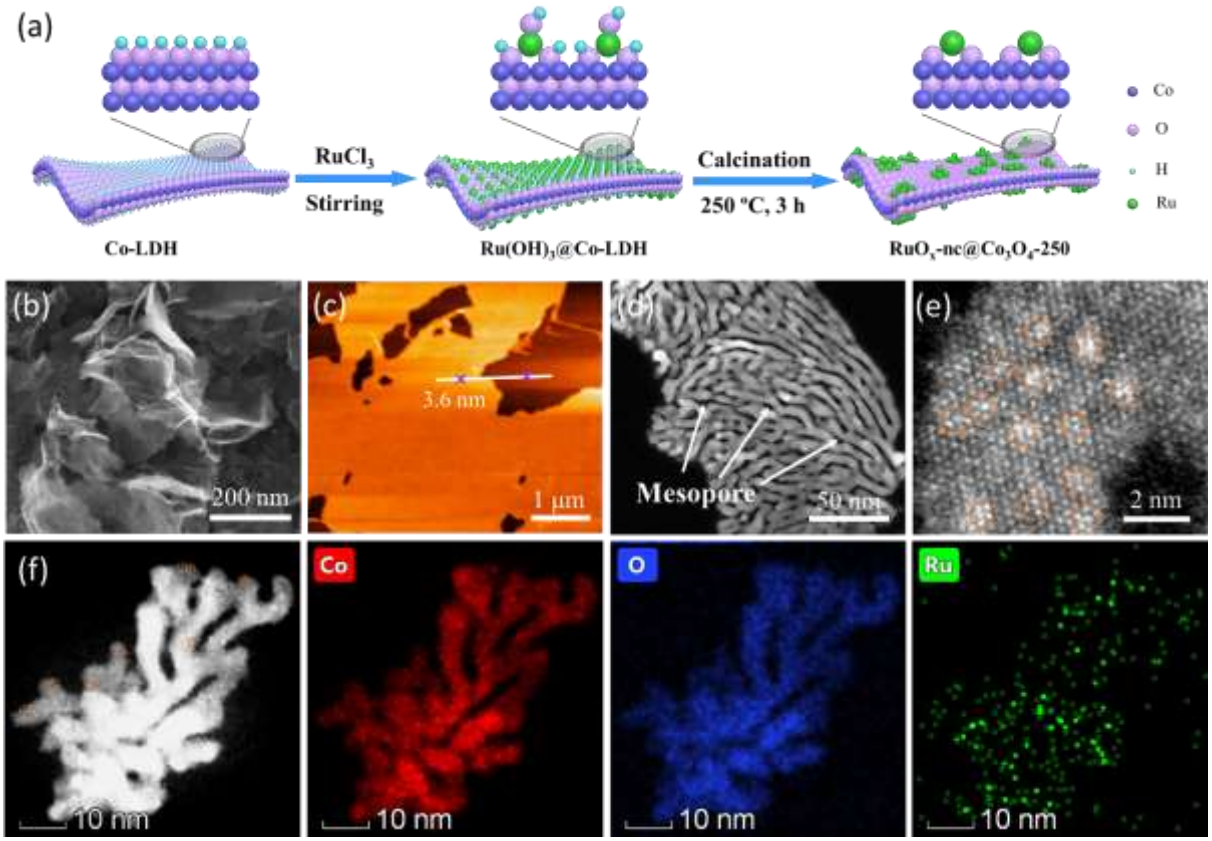

Figure 1. (a) Synthetic scheme, (b) SEM, (c) AFM, (d-f) HAADF STEM images and corresponding EDX mapping of RuO_x-nc@Co_3O_4-250.

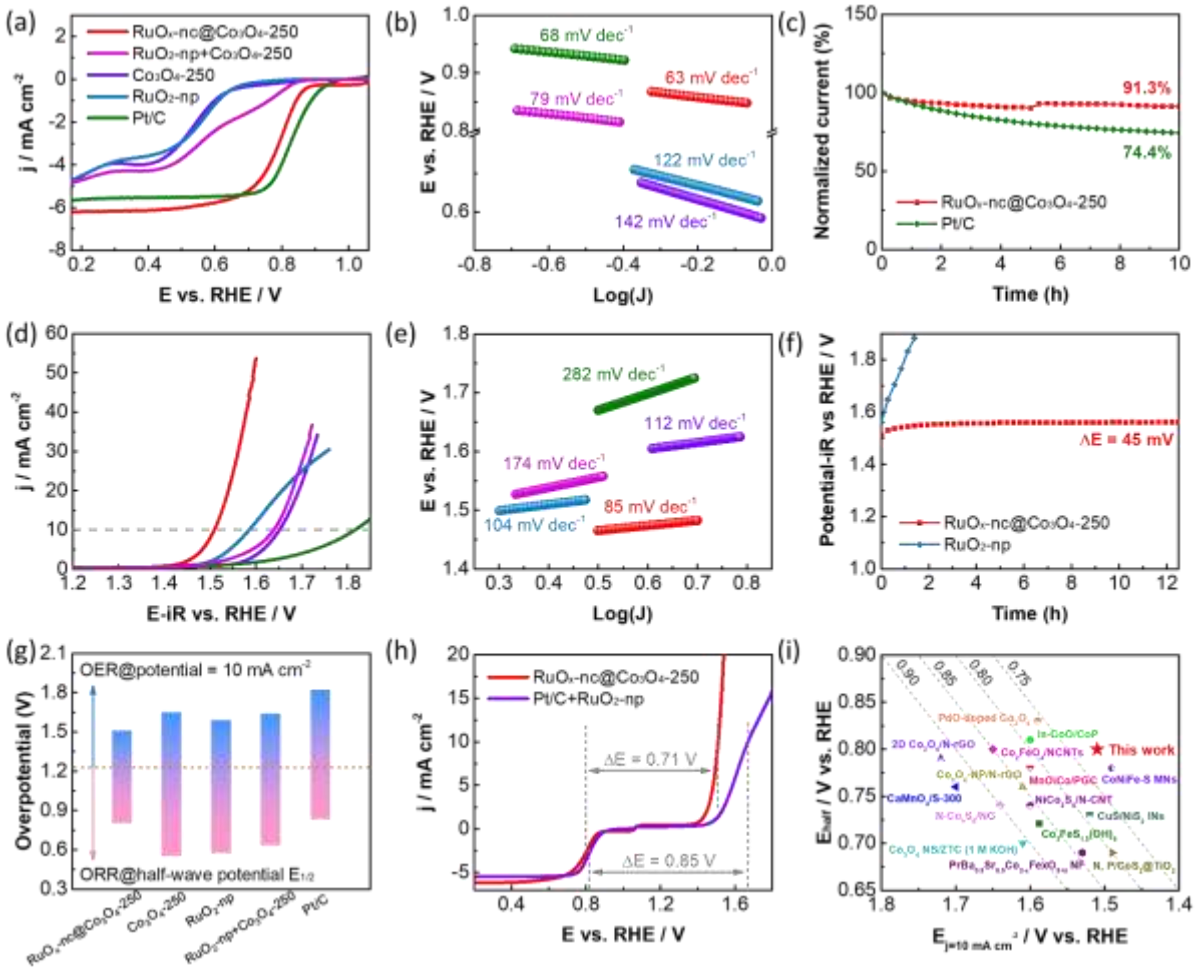

Figure 2. (a) LSV curves and (b) Tafel plots of ORR, (c) chronoamperometric response of ORR at 0.30 V (vs. RHE/V), (d) LSV curves and (e) Tafel plots of OER, (f) OER durability at 10 mA cm^{-2}, (g) the potential gap (ΔE) of different catalysts; (h) the overall LSV curves for bifunctional RuO_x-nc@Co_3O_4-250 and mixture of Pt/C+RuO_2-np, (i) the comparison of ORR and OER overpotentials for reported catalysts with this work ($\Delta E = E_{j=10\ mA\ cm^{-2}} - E_{j=-3mA\ cm^{-2}}$).

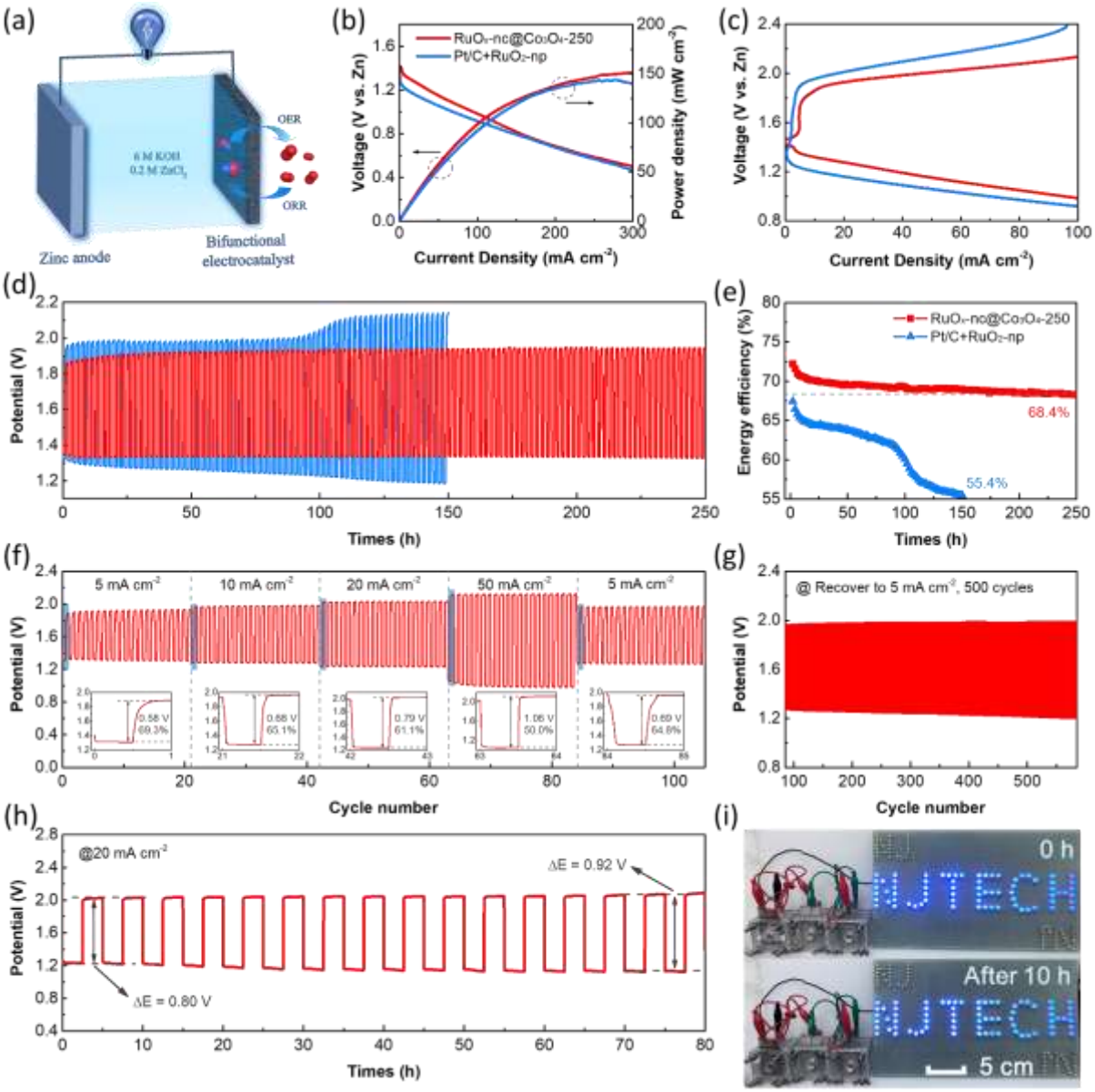

Figure 3. (a) Diagram of rechargeable Zn-air battery; (b) polarization (V-j) curves and power density (P-j) curves and (c) discharge/charge polarization curves based on the Pt/C+ RuO_2-np and RuO_x-nc@Co_3O_4-250 catalyst; (d) galvanostatic charge/discharge test at 2 mA cm^{-2} and (e) corresponding energy efficiency for Pt/C+RuO_2-np and RuO_x-nc@Co_3O_4-250; (f) galvanostatic charge/discharge test at different current densities (5-50 mA cm^{-2}) for RuO_x-nc@Co_3O_4-250, and (g) cycling performance after recovering to 5 mA cm^{-2} for 500 cycles; (h) galvanostatic charge/discharge test at 20 mA cm^{-2} for RuO_x-nc@Co_3O_4-250 catalyst; (i) three home-made rechargeable Zn-air batteries connected in series used to power a LED display screen.

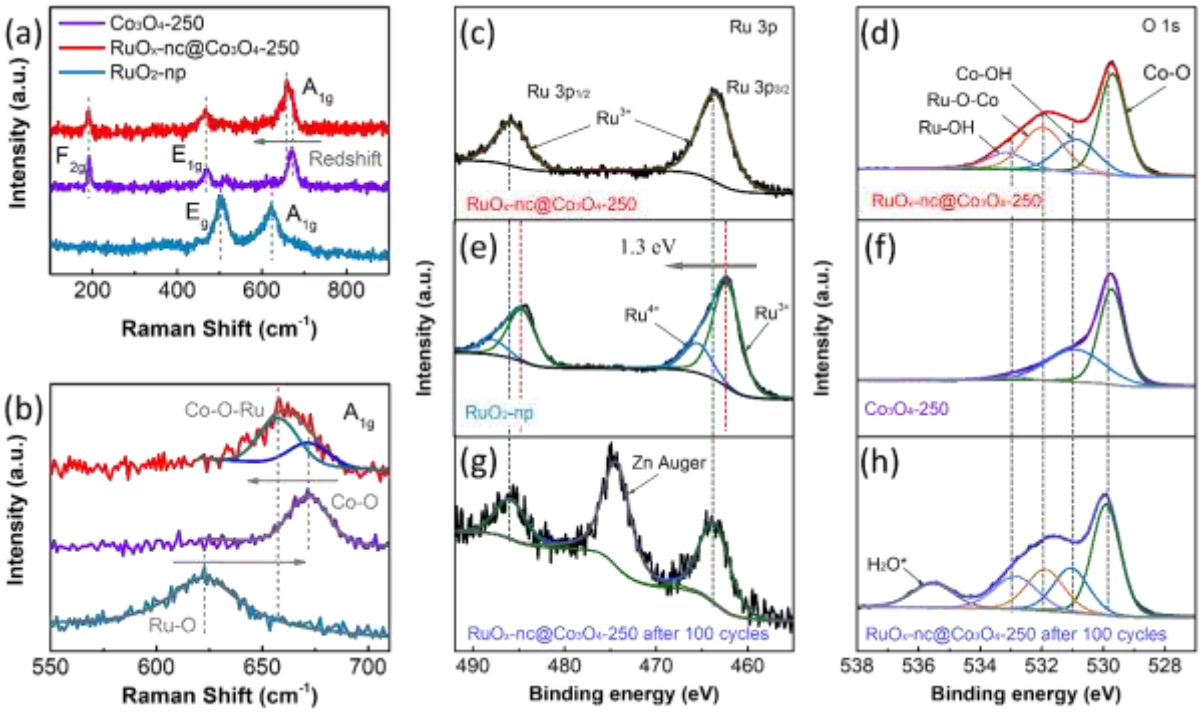

Figure 4. (a, b) Raman scattering spectra of RuO_x-nc@Co_3O_4-250, Co_3O_4-250, and RuO_2-np; XPS spectra of (c) Ru 3p and (d) O 1s for RuO_x-nc@Co_3O_4-250; XPS spectra of (e) Ru 3p for RuO_2-np and (f) O 1s for Co_3O_4-250; XPS spectra of (g) Ru 3p and (h) O 1s for RuO_x-nc@Co_3O_4-250 after 100 cycles at 10 mA cm^{-2} in Zn-air batteries.

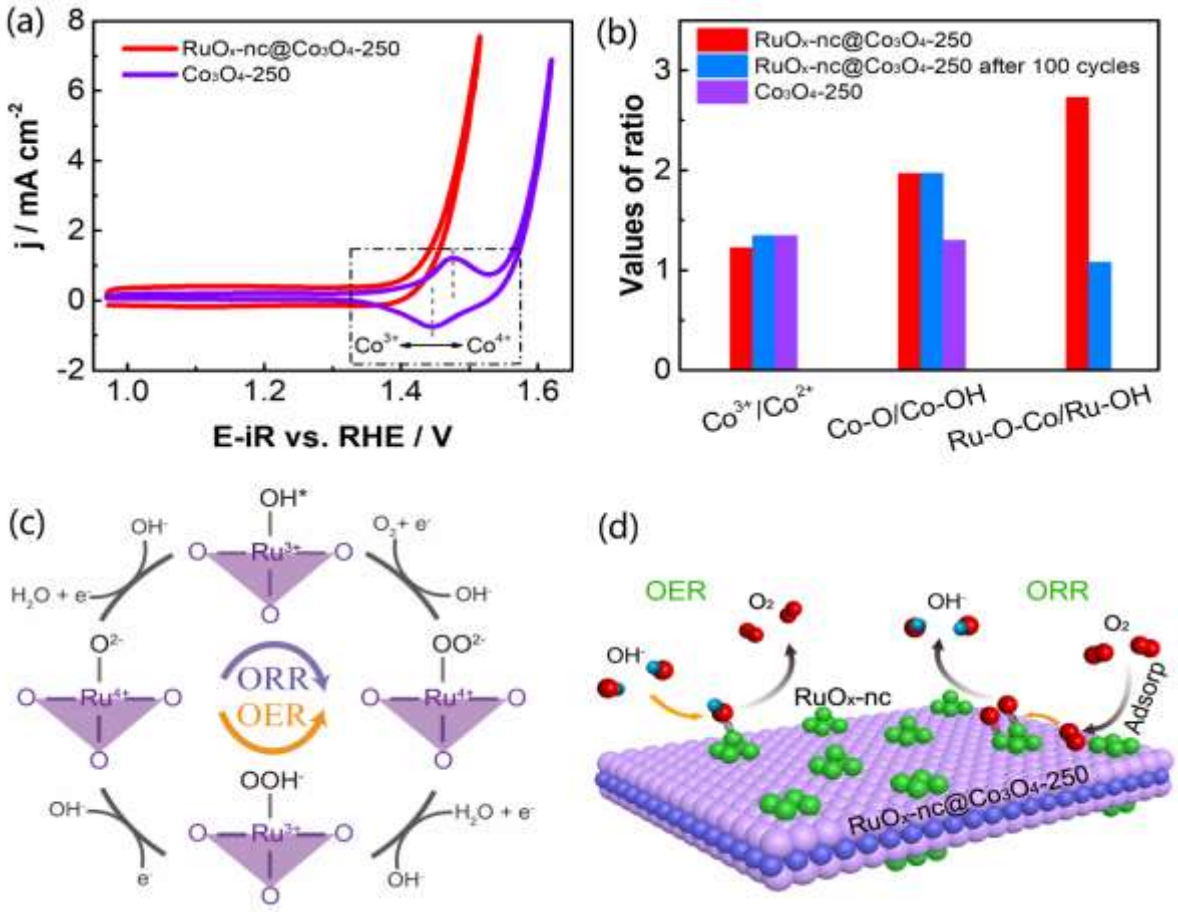

Figure 5. (a) CV curves of RuO_x-nc@Co_3O_4-250 and Co_3O_4-250 catalysts in 0.1 M KOH electrolyte with scan rate of 5 mV s^{-1}; (b) the comparison of the value of Co^{3+}/Co^{2+}, Co-O/Co-OH and Ru-O-Co/Ru-OH before and after cycling; (c) possible mechanism of the ORR (clockwise) and OER (anticlockwise) with RuO_x-nc@Co_3O_4-250; (d) schematic illustration of the proposed mechanism for the RuO_x-nc@Co_3O_4-250.